Journal of Catalysis **181,** 37–48 (1999)
Article ID jcat.1998.2290, available online at http://www.idealibrary.com on IDEAL®

Study of Gold Species in Iron-Oxide-Supported Gold Catalysts Derived from Gold-Phosphine Complex $Au(PPh_3)(NO_3)$ and As-Precipitated Wet $Fe(OH)_3^*$

Anguelina P. Kozlova,* Alexander I. Kozlov,* Sho Sugiyama,* Yoshio Matsui,† Kiyotaka Asakura,‡ and Yasuhiro Iwasawa*,[1]

*Department of Chemistry, ‡Research Center for Spectrochemistry, Graduate School of Science, The University of Tokyo, Hongo, Bunkyo-ku, Tokyo 113-0033, Japan; †National Institute for Research in Inorganic Materials, Namiki 1-1, Tsukuba, Ibaraki 305, Japan

Received June 8, 1998; revised September 18, 1998; accepted September 28, 1998

Iron-oxide-supported gold catalysts were prepared by supporting a Au phosphine complex $Au(PPh_3)(NO_3)$ on as-precipitated wet iron hydroxide $Fe(OH)_3^*$, followed by temperature-programmed calcination. The $Au/Fe(OH)_3^*$ catalysts calcined at the temperatures 573–773 K showed extremely high catalytic performance for CO oxidation at temperatures as low as 203–253 K. Interaction of the $Au(PPh_3)(NO_3)$ gold precursor with the $Fe(OH)_3^*$ upon supporting, transformation of the precursor during the heat treatments, and state of the gold in the catalysts were studied by FT-IR, XRD, TEM, XPS, and EXAFS. The gold precursor dissociated on the $Fe(OH)_3^*$ surface to produce $[Au(PPh_3)]^+$ species which partially decomposed at 473 K and was transformed to small gold metallic particles with coordination numbers of 7.4–8.0 for Au-Au bond at calcination temperatures $\geq$573 K. In contrast, decomposition of the gold complex over crystalline $Fe_2O_3^*$ resulted in large gold particles. The $Au/Fe_2O_3^*$ sample was inactive at 203–253 K and exhibited very low activity for CO oxidation at room temperature. The efficiency of the as-precipitated wet $Fe(OH)_3^*$ as a support is explained in terms of a higher stability of $[Au(PPh_3)]^+$ on the $Fe(OH)_3^*$ as compared to the $Fe_2O_3^*$ due to more effective interaction of the Au species with OH groups and defects of the amorphous $Fe(OH)_3^*$ surface. The results demonstrate the importance of support–metal precursor interactions, both upon supporting and during calcination, in the formation of highly active catalysts with small Au particles for low-temperature CO oxidation.

INTRODUCTION

Supported gold catalysts have attracted much attention in the field of both academic and industrial research. The renewal of the interest toward Au catalysis after the report of Ozin *et al.* on reactivity of matrix-trapped Au atom for CO oxidation at 30–40 K (1) was further promoted by the finding of the extremely high catalytic performance of finely dispersed Au particles prepared by a coprecipitation method for low-temperature CO oxidation by Haruta *et al.* (2–4). It has been shown that Au-based catalytic materials can be applied for a number of industrial and ecological reactions including water–gas shift reaction (5–7), hydrogenation (8), complete oxidation of hydrocarbons and CO (9–16), and NO reduction (17, 18).

Molecular metal complexes and clusters supported on metal oxides have been extensively studied as precursors for active metal particle catalysts (19–22). During the last two years, several publications were concerned with application of phosphine-stabilized Pt-Au clusters as precursors for Pt-Au bimetal catalysts dispersed on silica and alumina supports (23–25). Recently we have demonstrated that well-characterized Au-phosphine complexes and clusters such as $Au(PPh_3)(NO_3)$ and $Au_9[(PPh_3)_8](NO_3)_3$ can be successfully applied to obtain supported Au metallic particles on a variety of metal oxides (26–28). Both selections of appropriate gold complexes as metal precursors and application of as-precipitated wet metal hydroxides as support precursors allowed us to obtain highly active Au catalysts for low-temperature CO oxidation (26–28). The newly developed method for preparation of supported Au catalysts involves supporting the $Au(PPh_3)(NO_3)$ complex on the as-precipitated wet metal hydroxides $M(OH)_x^*$ (the asterisk stands for the freshly precipitated wet state of a metal hydroxide) followed by vacuum-drying at room temperature and temperature-programmed calcination in air. The supported Au catalyst derived from $Au(PPh_3)(NO_3)$ and $Fe(OH)_3^*$ (hereinafter $Au/Fe(OH)_3^*$) showed high CO conversion even at 203 K and was one of the most active Au catalysts reported until now (26–28). In a recent communication, Mathieson *et al.* adopted this approach to supporting an organometallic precursor $[Au(NO_3)(CNBu^t)]$ onto as-precipitated iron hydroxide to produce an efficient Au catalyst for CO oxidation (29).

It was suggested that effective interaction of the $Au(PPh_3)(NO_3)$ precursor with OH groups and defects of the support surface is responsible for the formation of the

[1] To whom all correspondence should be addressed. E-mail: iwasawa@chem.s.u-tokyo.ac.jp.

0021-9517/99 $30.00

highly active catalyst. The nature of active sites for CO activation in supported gold catalysts has been discussed in the literature (4, 17, 18, 30–33). Generally, both Au(I) and Au(0) sites can catalyze CO oxidation. Minico *et al.* suggested by FT-IR study that Au(I) is more active, but less stable than Au(0) in a noncalcined coprecipitated Au/Fe_2O_3 catalyst (31). On the other hand, to explain the high oxidation activity of calcined Au catalysts prepared by a coprecipitation method, catalytic processes at the boundary between small gold particles and metal oxide surface was proposed by Haruta *et al.* (4, 32). The hypothesis was supported by FT-IR study (33). In the course of our study, the $Au/Fe(OH)_3^*$ catalyst was found to be more active than the Au/Fe_2O_3 catalyst prepared by a coprecipitation method, and characterization of the support of the $Au/Fe(OH)_3^*$ catalyst was reported previously (27, 28). Further, investigation of Au-species in the active $Au/Fe(OH)_3^*$ catalyst is necessary for understanding the high activity. A detailed picture of active species may evolve in the study on such catalysts that are prepared by using a metal complex precursor with a definite structure (34, 35). A study on transformation of the complex $Au(PPh_3)(NO_3)$ during calcination may give a new insight into creation of the high catalytic performance of the $Au/Fe(OH)_3^*$ catalyst.

The present paper is mainly concerned with characterization of Au-species of the active $Au/Fe(OH)_3^*$ catalyst. Interactions of the gold precursor with $Fe(OH)_3^*$ and changes of Au species upon supporting and during temperature-programmed calcination have been studied by means of FT-IR, XRD, TEM, XPS, and EXAFS. The results are discussed in relation with the catalytic CO oxidation activities of the $Au/Fe(OH)_3^*$ catalysts calcined at various temperatures.

EXPERIMENTAL

Catalyst Preparation

A gold complex $Au(PPh_3)(NO_3)$ was synthesized from $Au(PPh_3)Cl$ (36) and $AgNO_3$ (Wako Chemicals, 99.8% min.), according to the literature (37); IR peaks (Nujol): 1499 and 1275 cm^{-1} (NO_3-ligand), and 1484, 1437, and 1103 cm^{-1} (PPh_3-ligand). Iron hydroxide $Fe(OH)_3^*$ (the asterisk $*$ denotes as-precipitated wet iron hydroxide) and iron oxide $Fe_2O_3^*$ (derived from $Fe(OH)_3^*$) were prepared as described earlier (28).

$Au/Fe(OH)_3^*$ samples were obtained by impregnation of the as-precipitated wet iron hydroxide $Fe(OH)_3^*$ with an acetone solution of the gold complex $Au(PPh_3)(NO_3)$, followed by evaporation under vacuum at RT. The sample thus obtained is denoted as $Au/Fe(OH)_3^*$ (RT). The sample was further treated by temperature-programmed calcination at a heating rate of 4 K min^{-1} up to given temperatures in a flow of air (30 ml min^{-1}). The catalysts thus calcined are denoted as $Au/Fe(OH)_3^*$ (temp.). Details of the preparation procedure were reported earlier (27, 28). The $Au/Fe_2O_3^*$ sample was obtained by impregnation of the $Fe_2O_3^*$ support with an acetone solution of $Au(PPh_3)(NO_3)$, followed by vacuum-drying at RT and temperature-programmed calcination to 673 K. The sample before the calcination is denoted as $Au/Fe_2O_3^*$ (RT) hereinafter.

PPh_3-treated $Fe(OH)_3^*$ (hereinafter denoted as $Fe(OH)_3^*\{P\}$) was prepared similarly to $Au/Fe(OH)_3^*$ by impregnation of $Fe(OH)_3^*$ with an acetone solution of triphenylphosphine instead of $Au(PPh_3)(NO_3)$, followed by the vacuum-drying and calcination procedures. Coprecipitated Au/Fe_2O_3 sample (denoted as Au/Fe_2O_3-copr) was obtained according to the literature (3, 4) as described previously (28).

Au loading was 3 wt% for the $Au/Fe(OH)_3^*$ and $Au/Fe_2O_3^*$ samples and 4.1 wt% for the coprecipitated Au/Fe_2O_3 sample, as analyzed by XRF.

Sample Characterization

XRD patterns were measured on a MAC Science M03XHF X-ray diffractometer with nickel-filtered Cu-K_α radiation operated at 40 kV and 20 mA using 0.5° divergence and scattering slits and a 0.30-mm receiving slit. The XRD patterns were recorded in the 2θ range of 5 to 80° with accumulation of five repetitions at a scanning speed 2° (2θ) min^{-1} with 0.025–0.04° step. To provide larger sensitivity for Au(111) peak, a narrow 2θ range, 37–40°, was measured applying a scanning speed of 1° (2θ) min^{-1} with an accumulation of 20 repetitions.

TEM images were observed on a Hitachi-1500 electron microscope operated at 800 kV. A small amount of a sample was ultrasonically dispersed in CCl_4 and a drop of the fine suspension was placed on a carbon-coated copper grid. To determine the size distribution of Au metal particles, TEM photographs were taken with 440,000 magnification.

XPS spectra were recorded on a Rigaku XPS 7000 spectrometer using a Mg-Kα source for excitation. A power setting of 10 kV and 20 mA was applied. The working pressure in an analyzing chamber was less than 5×10^{-7} Pa. XPS spectra for Au 4f, P 2p, and O 1s were measured applying 15 eV pass energy and 0.1 eV step energy. The observed binding energies (BE) were referred to 284.6 eV for C 1s level (38), which existed in all samples. For the XPS analysis, all sample specimens were obtained by pressing sample powders into thin disks which were mounted on sample holders and placed in a prechamber, outgassed to less than 1×10^{-6} Pa at room temperature, and then the sample disks were transferred to the analysis chamber. Stability of $Au(PPh_3)(NO_3)$ during the XPS measurements was proved by a series of successive measurements. The relative concentration (n_1/n_2) of two elements was estimated using Scofield's photoelectron cross sections (39).

Measurements of Au L_3-edge EXAFS spectra for the $Au/Fe(OH)_3^*$ and $Au/Fe_2O_3^*$ samples, subjected to various

heating treatments were performed at BL7C station in Photon Factory (PF) of Institute of Materials Structure Science (IMSS), High Energy Accelerator Research Organization (KEK), Proposal 97-G040. The EXAFS spectra were observed at room temperature in a transmission mode with an electron energy of 2.5 GeV and a beam current of 250–350 mA. A sagital-focusing Si(111) double crystal monochromator was used with a 50% detuning. Higher harmonics were removed by detuning of the parallelism of the two crystals. Two ionization chambers filled with N_2 and N_2/Ar (3 : 1) were used for I_o (incident X-ray intensity) and I (transmitted X-ray intensity), respectively. The samples for the measurements were pressed into self-supporting disks. The EXAFS data were analyzed by the EXAFS analysis program "Rigaku EXAFS (REX)." The background was removed by using a spline smoothing method in the range of 50 eV–700 eV above the edge and the extracted oscillation was normalized by the edge height, the energy dependence of which was estimated by the McMaster relation (40). The k^3-weighted $\chi(k)$ oscillations in the k range 30–123 nm^{-1} were Fourier transformed to r space. The curve-fitting analysis was carried out on inversely Fourier transformed data over 0.1–0.33 nm in r space. The empirical phase shift and amplitude functions for Au-P and Au-Au bonds were extracted from the EXAFS data for Au(PPh$_3$)(NO$_3$) and Au foil, respectively.

FT-IR spectra were measured on a JASCO FTIR 230 spectrometer in a transmission mode with 4 cm^{-1} resolution. The measurements were conducted in an *in-situ* IR cell combined in a closed circulating system at RT. Vacuum-dried samples were pressed into self-supported thin disks with a diameter of 2 cm. The samples were heated (4 K min^{-1}) under 13.3 kPa of O_2 from 298 K to given temperatures.

Catalytic Performance

Catalytic CO oxidation reactions were carried out in a glass fixed-bed flow reactor equipped with a computer-controlled auto-sampling system at atmospheric pressure; 1.0% CO balanced with air; SV = 20,000 ml h^{-1} g^{-1} (27, 28). The catalytic activity is expressed as the degree of CO conversion.

RESULTS

Catalytic CO Oxidation

Figure 1 shows the catalytic performance of Au/Fe(OH)$_3^*$ calcined at various temperatures, together with those for Au/Fe$_2$O$_3$-copr and Au/Fe$_2$O$_3^*$ (673 K). The Au/Fe(OH)$_3^*$ (RT) sample exhibited no activity for CO oxidation at room temperature. It was, however, observed that the Au/Fe(OH)$_3^*$ (473 K) sample was more active than Au/Fe$_2$O$_3^*$, but significantly less active than the Au/Fe$_2$O$_3$-copr catalyst. On the other hand, calcination of Au/Fe(OH)$_3^*$ at 573, 673, and 773 K produced catalysts with very high activity for CO oxidation. Au/Fe(OH)$_3^*$ (573 K) and Au/Fe(OH)$_3^*$ (673 K) showed almost identical catalytic performances with 80–83% CO conversions at 223 K. The catalytic activity of Au/Fe(OH)$_3^*$ (773 K) seemed slightly less, but was still remarkably high for the low-temperature CO oxidation.

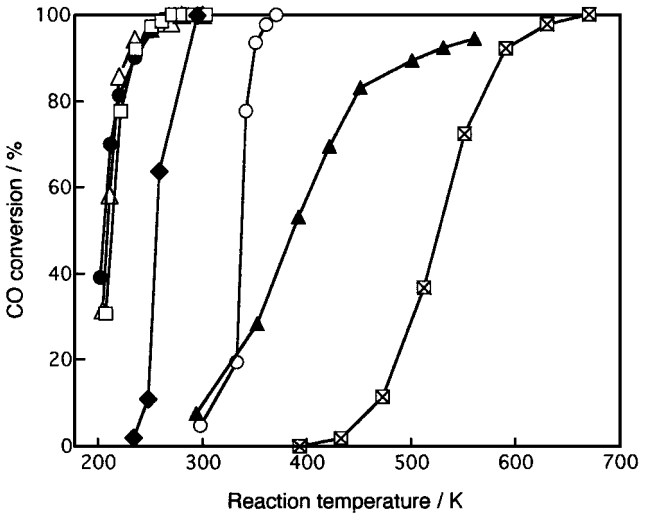

FIG. 1. Catalytic performance of the Au/Fe(OH)$_3^*$ samples after calcination at various temperatures, and the Au/Fe$_2$O$_3^*$, Au/Fe$_2$O$_3$-copr, and Fe(OH)$_3^*${P} samples calcined at 673 K: (–○–) Au/Fe(OH)$_3^*$ (473 K); (–△–) Au/Fe(OH)$_3^*$ (573 K); (–●–) Au/Fe(OH)$_3^*$ (673 K); (–□–) Au/Fe(OH)$_3^*$ (773 K); (–▲–) Au/Fe$_2$O$_3^*$ (673 K); (–⊠–) Fe(OH)$_3^*${P}; (–◆–) Au/Fe$_2$O$_3$-copr (673 K).

XRD Measurements

XRD patterns of Au/Fe(OH)$_3^*$ calcined at 473, 573, 673, and 773 K, and Au/Fe$_2$O$_3^*$ are shown in Fig. 2. The

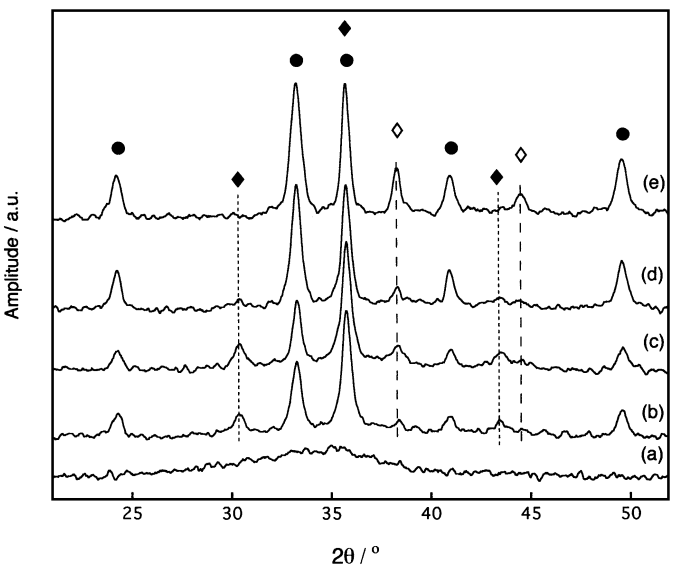

FIG. 2. XRD patterns of the Au/Fe(OH)$_3^*$ samples after calcination for 4 h at (a) 473 K, (b) 573 K, (c) 673 K, (d) 773 K, and (e) the Au/Fe$_2$O$_3^*$ sample calcined at 673 K for 4 h; ◇, Au; ◆, γ-Fe$_2$O$_3$; ●, α-Fe$_2$O$_3$.

$Au/Fe(OH)_3^*$ (473 K) catalyst was amorphous without any definite XRD peak (Fig. 2a). Noticeable changes in the sample crystallinity occurred upon increasing the calcination temperature to 573–773 K. XRD peaks corresponding to α-Fe_2O_3, γ-Fe_2O_3, and Au metallic phase were detected in Figs. 2b–2d. The $Au/Fe_2O_3^*$ catalyst revealed relatively strong XRD peaks due to Au metallic phase (Fig. 2e), where the mean size of the gold crystallites was calculated to be about 20 nm by the Scherrer equation. It should be noted that intensities of the Au(111) and Au(200) reflections in $Au/Fe(OH)_3^*$ (573 K), $Au/Fe(OH)_3^*$ (673 K), and $Au/Fe(OH)_3^*$ (773 K) were significantly lower than those for $Au/Fe_2O_3^*$.

TEM Observations

The size distributions of Au metallic particles in the $Au/Fe(OH)_3^*$ (673 K) and $Au/Fe_2O_3^*$ were estimated by TEM. The histograms of the Au metallic particle distributions are shown in Fig. 3. The histogram of the size distribution in the $Au/Fe(OH)_3^*$ (673 K) catalyst revealed relatively narrow distribution feature (Fig. 3a), as compared with that for the $Au/Fe_2O_3^*$ catalyst which showed the broad size range up to 50 nm (Fig. 3b). The mean diameter size distribution of Au particles in the $Au/Fe(OH)_3^*$ (673 K) catalyst in Fig. 3a was similar to that determined in our previous study (27), demonstrating good reproducibility of independent preparations of the $Au/Fe(OH)_3^*$ samples. The average Au particle sizes ($\bar{d}$) for $Au/Fe(OH)_3^*$ (673 K) and $Au/Fe_2O_3^*$ were determined to be 2.6 nm and 12 nm, respectively.

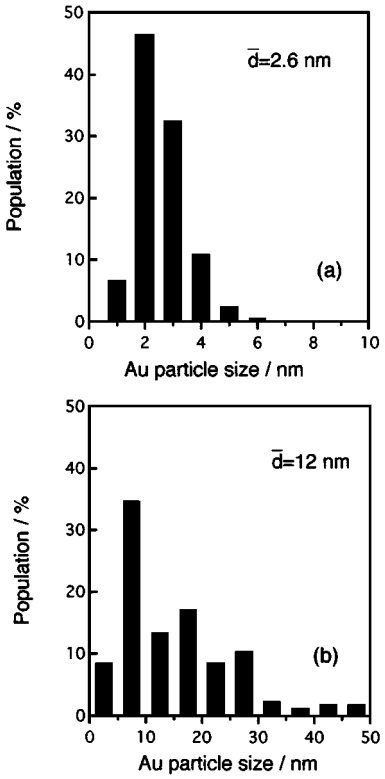

FIG. 3. Size distributions of Au metallic particles in (a) $Au/Fe(OH)_3^*$ (673 K) and (b) $Au/Fe_2O_3^*$ (673 K) estimated by TEM.

TABLE 1

The XPS Binding Energies of Au $4f_{7/2}$, P 2p, and O 1s, and the Au/P, Fe/Au, and Fe/P Ratios for $Au/Fe(OH)_3^*$, $Au/Fe_2O_3^*$, $Fe(OH)_3^*${P}, and References

Sample (treatment temp.)	Binding energy, eV			Au/P ratio	Fe/Au ratio	Fe/P ratio
	Au $4f_{7/2}$	P 2p	O 1s			
$Au/Fe(OH)_3^*$						
(RT)	84.9	131.7	530.1	0.90	83	75
(473 K)	84.1	132.6	529.8	0.51	102	52
(673 K)	83.9	133.4	529.9	0.35	71	25
$Fe(OH)_3^*${P}						
(RT)	—	132.7	529.7	—	—	77
(473 K)	—	132.7	529.9	—	—	68
(673 K)	—	133.3	529.9	—	—	25
$Au/Fe_2O_3^*$						
(RT)	84.9	131.7	530.1	0.96	27	26
(673 K)	83.9	133.4	530.1	0.36	72	26
$Au(PPh_3)(NO_3)$	84.9	131.7	532.2	0.94	—	—
$Ph_3P{=}O$	—	132.1	531.9	—	—	—

XPS Measurements

Table 1 summarizes the results of the XPS measurements for several Au-containing samples and reference compounds. The Au 4f and P 2p XPS spectra for the $Au/Fe(OH)_3^*$ and $Au/Fe_2O_3^*$ catalysts are shown in Fig. 4.

In the Au 4f region, the $Au/Fe(OH)_3^*$ catalyst before calcination showed the Au $4f_{7/2}$ peak at 84.9 eV with FWHM of 2.0 eV. The binding energy (BE) value reflects a Au(+1) state and coincides with that for the complex $Au(PPh_3)(NO_3)$ (Table 1). Calcination of the $Au/Fe(OH)_3^*$ sample at 473 K caused a shift of the Au $4f_{7/2}$ peak position and a broadening of the peak toward lower BE values. The Au $4f_{7/2}$ peak with FWHM of 2.2 eV was centered at about 84.1 eV. Predominant peaks in the XPS Au 4f spectra for both $Au/Fe(OH)_3^*$ and $Au/Fe_2O_3^*$ samples calcined at 673 K have a BE of 83.9 eV which is characteristic of metallic Au, and the FWHM was 1.6 eV.

The broad P 2p peak for the $Au/Fe(OH)_3^*$ (RT) sample before calcination was centered at 131.7 eV. The BE value corresponds to that for the complex $Au(PPh_3)(NO_3)$ (Table 1). Upon calcination at 473 and 673 K, the P 2p peak shifted towards higher BE values. The BE value of 132.6 eV for $Au/Fe(OH)_3^*$ (473 K) was similar to those (132.7 eV) for PPh_3-treated $Fe(OH)_3^*${P} before and after calcination at 473 K as shown in Table 1. The data demonstrate that PPh_3 is not oxidized until 473 K when supported on $Fe(OH)_3^*$. Calcination at 673 K caused a shift of the P 2p BE to 133.4 eV for $Au/Fe(OH)_3^*$, and to 133.3 eV for $Fe(OH)_3^*${P}. The high BE value indicates the formation of oxygen-containing

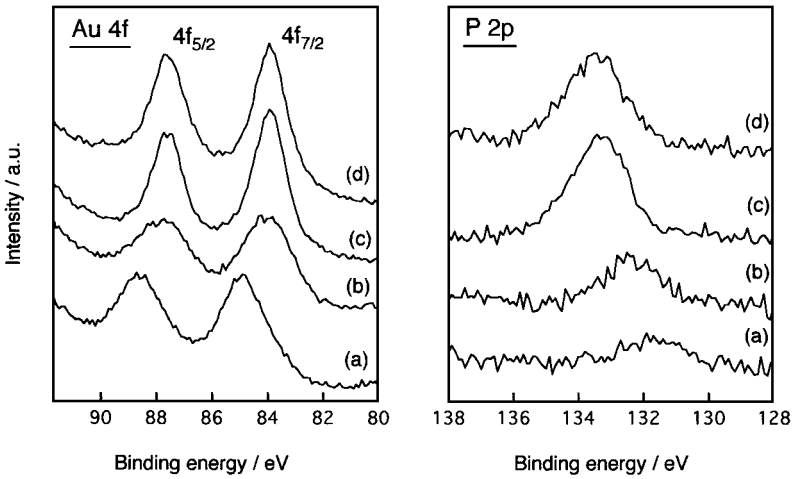

FIG. 4. XPS Au 4f and P 2p spectra of (a) Au/Fe(OH)$_3^*$ (RT), (b) Au/Fe(OH)$_3^*$ (473 K), (c) Au/Fe(OH)$_3^*$ (673 K), and (d) Au/Fe$_2$O$_3^*$ (673 K).

phosphorus species other than phosphine oxide $PPh_3P{=}O$ with BE of 132.1 eV or P_2O_5 with BE of 135 eV (38).

Transformations of both Au and P species in the Au/Fe(OH)$_3^*$ sample during the calcinations were also reflected in the changes of the Au/P, Fe/P, and Fe/Au ratios as shown in Table 1. Both Au/Fe(OH)$_3^*$ (RT) and Au/Fe$_2$O$_3^*$ (RT) showed the Au/P ratios close to that for Au(PPh$_3$)(NO$_3$). Gold aggregation occurred during calcinations at 473 and 673 K (supported by EXAFS described below) and led to the decrease of the Au/P ratio. As the Fe(OH)$_3^*$ support crystallized simultaneously with the above change (28), the Fe/P ratio in Au/Fe(OH)$_3^*$ also decreased upon the calcination. The Fe/P ratios for the Au/Fe(OH)$_3^*$ (RT), Au/Fe(OH)$_3^*$ (473 K), and Au/Fe(OH)$_3^*$ (673 K) samples were similar to those for the corresponding Fe(OH)$_3^*${P} samples. The Fe/Au ratio increased a little by calcination at 473 K and decreased by calcination at 673 K. The Au/P, Fe/P, and Fe/Au ratios for Au/Fe(OH)$_3^*$ (673 K) were similar to those for Au/Fe$_2$O$_3^*$ (673 K), in which gold atoms are supported on the surface.

EXAFS Measurements

Figures 5 and 6 show k^3-weighted Fourier transforms for the EXAFS data at Au L$_3$-edge for Au/Fe(OH)$_3^*$ and Au/Fe$_2$O$_3^*$, respectively, together with reference spectra of Au foil and Au(PPh$_3$)(NO$_3$). In the Fourier transform for the complex Au(PPh$_3$)(NO$_3$), a peak was observed at 0.18 nm (phase shift uncorrected) which is assigned to the Au-P bond (41). Similar Fourier transforms were obtained for the Au/Fe(OH)$_3^*$ (RT) and Au/Fe$_2$O$_3^*$ (RT) samples as shown in Fig. 5 and Fig. 6. Curve-fitting analysis for the EXAFS data was carried out assuming $N = 1$ and $r = 0.220$ nm for the Au-P bond in Au(PPh$_3$)(NO$_3$). Results of the curve-fitting analysis are shown in Fig. 7. Distances and coordination numbers for the Au-P bond were 0.221 ± 0.002 nm and 1.3 ± 0.3 for Au/Fe(OH)$_3^*$ (RT), and 0.222 ± 0.002 nm and 1.1 ± 0.3 for Au/Fe$_2$O$_3^*$ (RT) (Table 2). The results allow us to suppose that the gold precursor was not decomposed after supporting, on both Fe(OH)$_3^*$ and Fe$_2$O$_3^*$ at RT.

Curve-fitting analysis for the EXAFS data at the Au L$_3$-edge for the Au/Fe(OH)$_3^*$ samples after calcination at 473, 573, 673, and 773 K is presented in Fig. 7A and

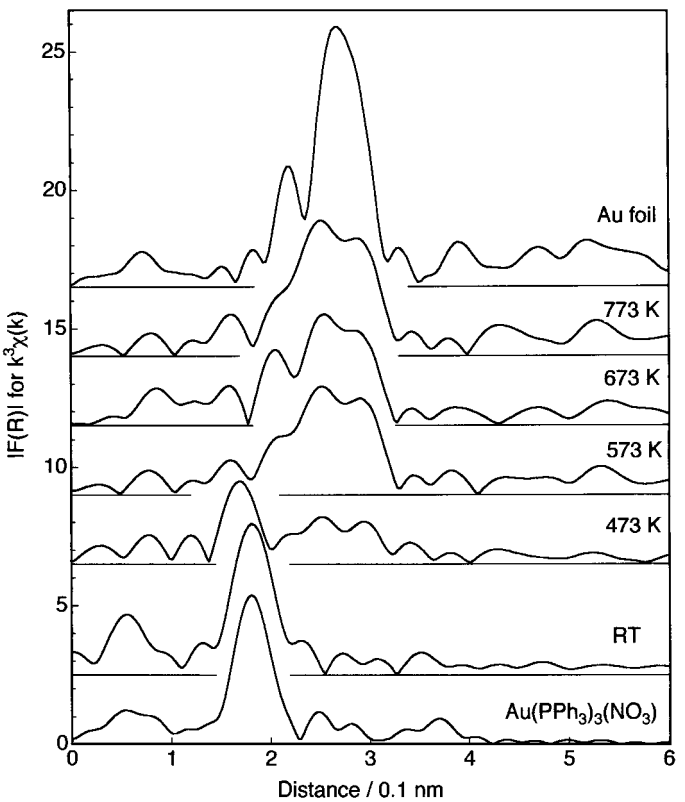

FIG. 5. Fourier transforms for the Au L$_3$-edge EXAFS data for Au/Fe(OH)$_3^*$ at RT and after calcination at 473, 573, 673, and 773 K; Au foil and Au(PPh$_3$)(NO$_3$).

TABLE 2

The Best Curve-Fit Results for the Au L_3-Edge EXAFS Data of $Au(PPh_3)(NO_3)$ Before and After Supporting on $Fe(OH)_3^*$ and $Fe_2O_3^*$ Followed by Vacuum-Drying at RT

Sample	Bond	N	r/nm	$\Delta\sigma^2/10^{-6}$ nm^2	ΔE/eV
$Au(PPh_3)(NO_3)$	Au-P	(1)	(0.220)	(0.0)	(0.0)
$Au/Fe(OH)_3^*$ (RT)	Au-P	1.3 ± 0.3	0.221 ± 0.002	1.0 ± 3	0.6 ± 3
$Au/Fe_2O_3^*$ (RT)	Au-P	1.1 ± 0.3	0.222 ± 0.002	1.1 ± 3	1.5 ± 3

Note. N: coordination number, *r*: bond distance, σ: Debye Waller factor, ΔE: difference in the origin of photoelectrons between the sample and the reference.

the best-fit results are shown in Table 3. The k^3-weighted Fourier transforms are given in Fig. 5. Calcination of the $Au/Fe(OH)_3^*$ sample at 473 K caused a decrease in intensity of the peak around 0.18 nm in the Fourier transform, and the peak at 0.2–0.3 nm appeared simultaneously. The curve-fitting analysis revealed the presence of both Au-P and Au-Au bonds at the distances of 0.220 ± 0.003 nm (coordination number: 0.6 ± 0.3) and 0.287 ± 0.003 nm (coordination number: 2.2 ± 1.5), respectively (Table 3). Increase of the calcination temperature to 573 K caused complete disappearance of the Au-P bond (Table 3) and further development of Au-Au peak at about 0.27 nm in the Fourier transform of Fig. 5. Heating of the $Au/Fe(OH)_3^*$ sample at 673 and 773 K led to a small increase in the Au-Au peak intensity in Fig. 5 and in the coordination number of the Au-Au bond, in comparison with those for $Au/Fe(OH)_3^*$ (573 K) sample (Table 3). The Au-Au bond distances for $Au/Fe(OH)_3^*$ (573 K), $Au/Fe(OH)_3^*$ (673 K), and $Au/Fe(OH)_3^*$ (773 K) were 0.286–0.287 nm which are essentially the same as 0.287 nm for Au foil, but the coordination numbers were in the range of 7.4–8.0, which are significantly smaller than 12 for Au foil (Table 3).

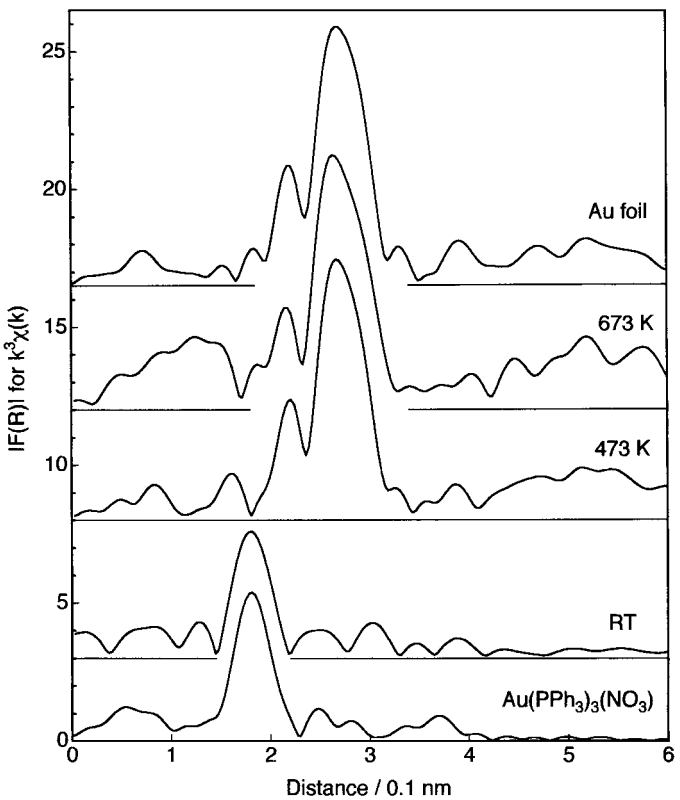

FIG. 6. Fourier transforms for the Au L_3-edge EXAFS data for $Au/Fe_2O_3^*$ at RT and after calcination at 473 and 673 K; Au foil and $Au(PPh_3)(NO_3)$.

Curve-fitting analysis for the EXAFS data at the Au L_3-edge for the $Au/Fe_2O_3^*$ samples after calcination at 473 and 673 K is presented in Fig. 7B and the best-fit results are shown in Table 3. The k^3-weighted Fourier transforms are given in Fig. 6. Intensity and position of the peak in the Fourier transforms for the $Au/Fe_2O_3^*$ (473 K) and $Au/Fe_2O_3^*$ (673 K) samples were very close to those for Au foil. No Au-P bond was observed. Curve-fitting analysis of the EXAFS data proved that in the $Au/Fe_2O_3^*$ (473 K) and $Au/Fe_2O_3^*$ (673 K) samples large Au metallic particles (coordination numbers of 12 ± 1.0, and 12 ± 1.5, respectively) were formed (Fig. 7B, Table 3).

FT-IR Measurements

Figure 8 shows the FT-IR spectra for $Au(PPh_3)(NO_3)$ and $Au/Fe(OH)_3^*$ (RT). The complex $Au(PPh_3)(NO_3)$ in

TABLE 3

The Best Curve-Fit Results for the Au L_3-Edge EXAFS Data of $Au/Fe(OH)_3^*$ and $Au/Fe_2O_3^*$ Calcined at Various Temperatures

Sample	Bond	N	r/nm	$\Delta\sigma^2/10^{-6}$ nm^2	ΔE/eV
$Au/Fe(OH)_3^*$					
473 K	Au-Au	2.2 ± 1.5	0.287 ± 0.003	8 ± 10	0 ± 3
	Au-P	0.6 ± 0.3	0.220 ± 0.003	6 ± 5	0 ± 4
573 K	Au-Au	7.4 ± 1.0	0.286 ± 0.002	13 ± 10	1 ± 4
673 K	Au-Au	7.9 ± 1.2	0.287 ± 0.002	18 ± 10	2 ± 3
773 K	Au-Au	8.0 ± 1.0	0.286 ± 0.002	5 ± 8	0 ± 4
$Au/Fe_2O_3^*$					
473 K	Au-Au	12 ± 1.0	0.287 ± 0.002	0 ± 8	0 ± 4
673 K	Au-Au	12 ± 1.5	0.287 ± 0.002	0 ± 8	1 ± 4

Note. N, *r*, σ, and ΔE: the parameters described in Table 2.

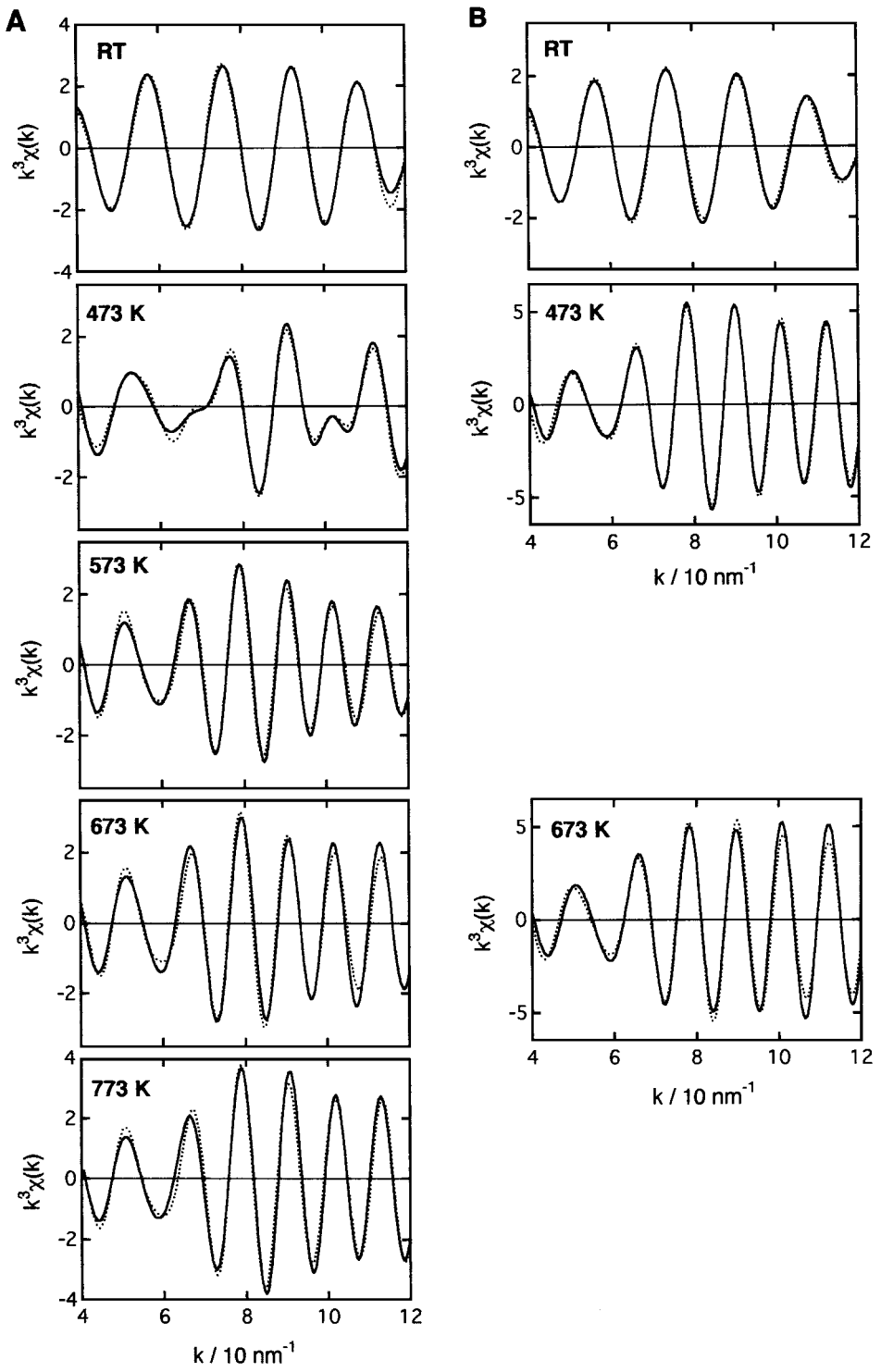

FIG. 7. The curve-fitting analysis of the EXAFS Au L_3-edge data for Au/Fe(OH)$_3^*$ (A) and Au/$Fe_2O_3^*$ (B) samples; (———) observed, (····) calculated.

Nujol showed strong absorption bands at 1499, 1484, 1437, 1275, and 1103 cm^{-1}. The bands at 1499 and 1275 cm^{-1} are characteristic of a NO_3-ligand in Au(PPh_3)(NO_3) and disappeared after supporting on Fe(OH)$_3^*$ as shown in Fig. 8 for the Au/Fe(OH)$_3^*$ (RT) sample. The broad bands centered at about 1360 and 1480 cm^{-1} in the FT-IR spectrum for Au/Fe(OH)$_3^*$ (RT) are referred to carbonate and nitrate contaminations resulting from Fe(OH)$_3^*$ synthesis (28, 42,

43). The former band hides a peak around 1380–1350 cm^{-1} for NO_3^- species which may be produced by the dissociative adsorption of $Au(PPh_3)(NO_3)$ on $Fe(OH)_3^*$. In fact, a strong and sharp IR band at 1363 cm^{-1} assignable to ionic NO_3^- species was clearly observed for $Au(PPh_3)(NO_3)$ supported on $Ti(OH)_4^*$ (48), prepared by aqueous hydrolysis of $Ti(i\text{-}OC_3H_7)_4$ as reported previously (27). It should be noted that no significant shift for the PPh_3-ligand bands at 1484, 1437, and 1103 cm^{-1} was observed upon supporting the Au-complex on $Fe(OH)_3^*$ and drying at RT.

In-situ FT-IR spectra for $Fe(OH)_3^*$ under heating treatments are also shown in Fig. 9 for comparison. Two IR-regions at 1000–1850 (H_2O-bending and ligand-region) and 2600–3890 cm^{-1} (OH-region) can be compared in Fig. 8 and Fig. 9. The intense band at about 1639 cm^{-1} (H_2O bending) and broad absorption in the region 2600–3650 cm^{-1}, due to hydrogen-bonded hydroxyls and adsorbed H_2O, demonstrate the presence of a large amount of physisorbed water and the different nature of OH groups in both vacuum-dried $Au/Fe(OH)_3^*$ (RT) and $Fe(OH)_3^*$ (RT) samples. Heating the samples at 423 K led to the removal of most of water that was monitored by disappearance of the band at 1639 cm^{-1} and to a remarkable decrease of the intensity in the 2600–3650 cm^{-1} region. Carbonate and nitrate contaminations also decreased upon heating at 423 K. In Fig. 8, sharp IR bands at 1102, 1437, and 1480 cm^{-1} due to PPh_3-ligand in $Au/Fe(OH)_3^*$ remained unchanged at calcination temperatures 423–473 K. At 523 K, the intensities of the bands decreased significantly and a band at about 1126 cm^{-1} appeared. The band may be ascribed to the formation of oxygen-containing phosphine compounds such as $Ph_3P{=}O$ (44). After heating the $Au/Fe(OH)_3^*$ sample at 573 K, the band at 1126 cm^{-1}, as well as the PPh_3-bands at 1102, 1437, and 1480 cm^{-1} disappeared completely. A broad band centered at 1060 cm^{-1} developed simultaneously and remained almost unchanged after heating at 673 K. Position and broad shape of the band allowed us to suggest the formation of inorganic phosphorus-containing ions on the $Au/Fe(OH)_3^*$ sample at 573 K (45).

As shown in Fig. 9, heating the $Fe(OH)_3^*$ support at 423 K made the hydroxyl band at 3640 cm^{-1} visible (46, 47). The band position changed by 10 cm^{-1} upon calcination at 573 K, and the band finally disappeared after heating at 673 K. In the case of the $Au/Fe(OH)_3^*$ samples heated at 423 and 473 K (Fig. 8), the OH-band shifted by 55 cm^{-1}, as compared to the band for the corresponding $Fe(OH)_3^*$.

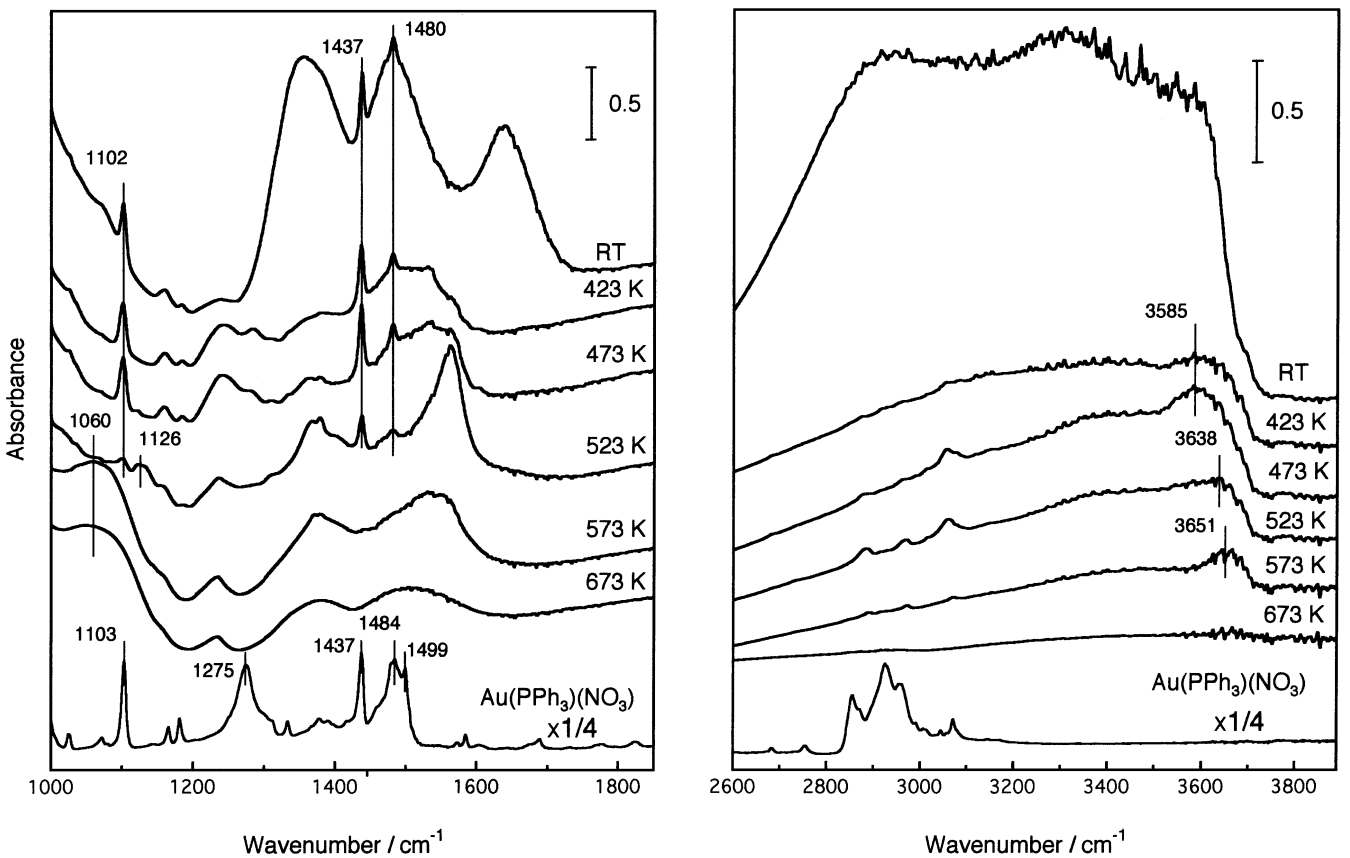

FIG. 8. FT-IR spectra for the $Au/Fe(OH)_3^*$ samples before calcination (RT) and after calcination at 423, 473, 523, 573, and 673 K, and for $Au(PPh_3)(NO_3)$ in Nujol.

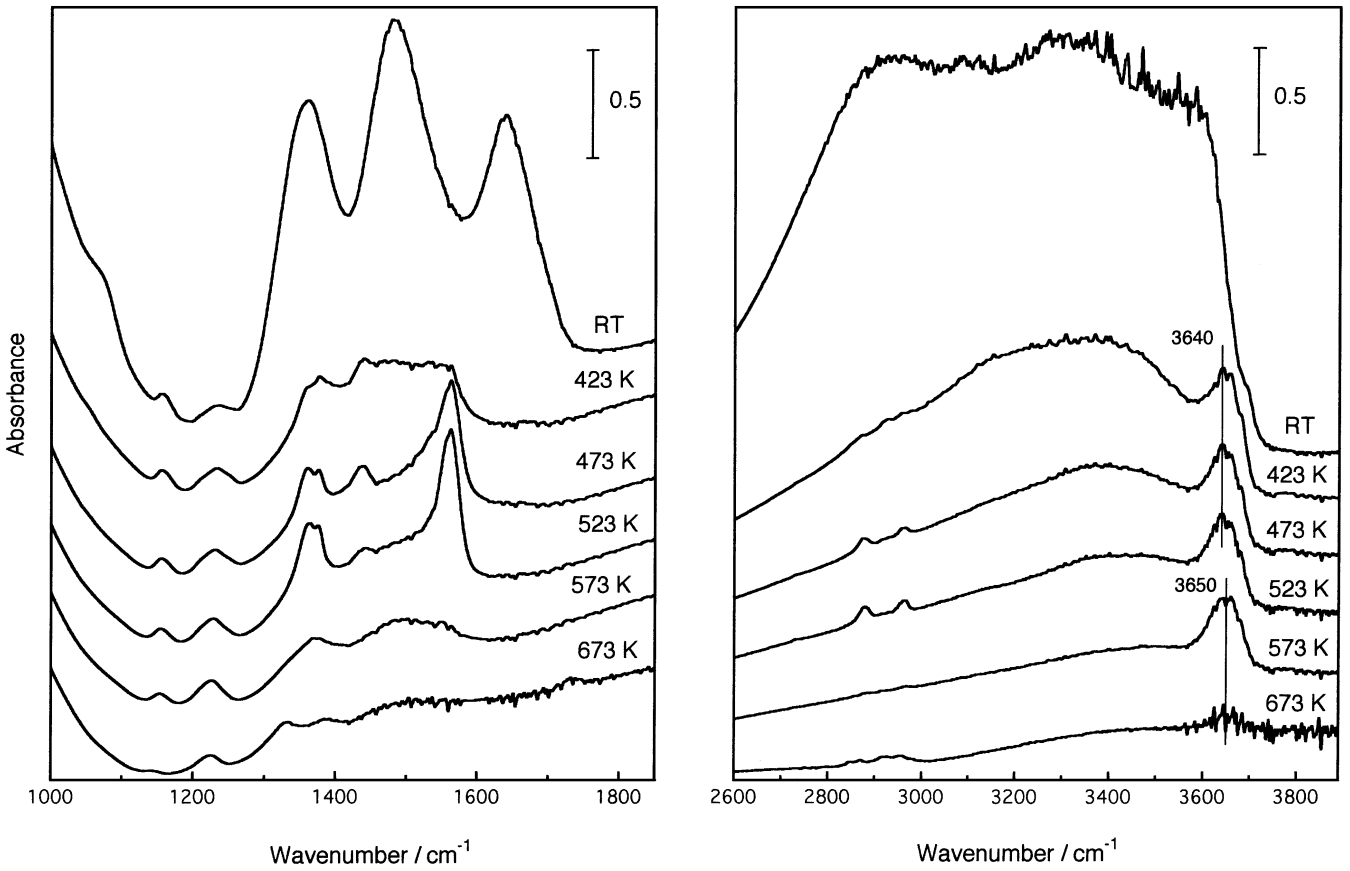

FIG. 9. FT-IR spectra of Fe(OH)$_3^*$ supports before calcination (RT) and after calcination at 423, 473, 523, 573, and 673 K.

After further heating of the Au/Fe(OH)$_3^*$ sample to 523 and 573 K, the OH-band position shifted to 3651 cm^{-1} similar to 3650 cm^{-1} for Fe(OH)$_3^*$ (573 K).

DISCUSSION

Interaction of Au(PPh$_3$)(NO$_3$) with Support

Metal-organic complexes are capable of reacting directly with surface hydroxyls of inorganic oxides to form chemical bonds. In the Au(PPh$_3$)(NO$_3$) complex, coordination of the nitrate anion is much weaker than that of the triphenylphosphine ligand. Supporting Au(PPh$_3$)(NO$_3$) on as-precipitated wet Fe(OH)$_3^*$ revealed the disappearance of the 1499 and 1275 cm^{-1} bands, which are characteristic of the NO$_3$-ligand in Au(PPh$_3$)(NO$_3$), as shown in Fig. 8. The results demonstrate the release of the NO$_3$-ligand from the complex upon supporting at RT. However, large IR absorbance of carbonate and nitrate impurities in the Fe(OH)$_3^*$ support did not allow us to detect definitely ionic NO_3^- species on the Au/Fe(OH)$_3^*$ (RT) sample. On the other hand, fortunately in the Au/Ti(OH)$_4^*$ (RT) sample the strong and sharp IR band at 1363 cm^{-1} due to ionic NO_3^- species on the support was observed clearly (48). The existence of an interaction between the gold precursor and the surface OH groups of Fe(OH)$_3^*$ was suggested from the previous FT-IR study (28). As one can see from Fig. 8 and Fig. 9, a 55 cm^{-1} shift of ν_{OH} was observed for the Au/Fe(OH)$_3^*$ samples calcined at 423 and 473 K, as compared with the corresponding Fe(OH)$_3^*$ support, while no shift of ν_{OH} was detected when [Au(PPh$_3$)]$^+$ unit was destroyed at 573 K. Consequently, we suppose that the gold complex precursor dissociates on the surface of Fe(OH)$_3^*$ to release the weakly coordinated NO$_3$ ligand and to produce the [Au(PPh$_3$)]$^+$ species that interacted electrostatically with the Fe(OH)$_3^*$ surface. Such a kind of support–metal precursor interaction at the initial stage of catalyst preparation seems to be important to obtain active gold catalysts with small Au particles.

The Au 4f and P 2p XPS BE values for Au/Fe(OH)$_3^*$ (RT) sample were the same as those for the Au(PPh$_3$)(NO$_3$) complex (Fig. 4 and Table 1). Further, the Au/P ratio in Au/Fe(OH)$_3^*$ (RT) resembled that in Au(PPh$_3$)(NO$_3$) (Table 1). These results indicate intact retention of the [Au(PPh$_3$)]$^+$ unit in the Au/Fe(OH)$_3^*$ (RT) sample. Curve-fitting analysis of the EXAFS Au L$_3$-edge data for Au/Fe(OH)$_3^*$ (RT) gave the Au-P bond distance and coordination number similar to those for the unsupported complex (Table 2). Thus, retention of the [Au(PPh$_3$)]$^+$ unit upon supporting of

$Au(PPh_3)(NO_3)$ on $Fe(OH)_3^*$ at RT was proved by the FT-IR, XPS, and EXAFS measurements.

The Fe/Au and Fe/P ratios estimated from the XPS spectra for $Au/Fe(OH)_3^*$ (RT) were much larger than those for $Au/Fe_2O_3^*$ (RT) as shown in Table 1. The Fe/P ratio for $Au/Fe(OH)_3^*$ (RT) was almost the same as that for $Fe(OH)_3^*\{P\}$ (Table 1). As the Au and P species in $Au/Fe_2O_3^*$ (RT) are supported on the $Fe_2O_3^*$ surface, the Fe/Au and Fe/P ratios in $Au/Fe(OH)_3^*$ (RT) being larger than in $Au/Fe_2O_3^*$ (RT) suggest that the majority of Au-phosphine species are located below the $Fe(OH)_3^*$ surface, such as in the pore channels of $Fe(OH)_3^*$. The supporting feature may reflect the stronger interaction of $Au(PPh_3)(NO_3)$ with the as-precipitated wet $Fe(OH)_3^*$, as compared with the interaction with the 673 K-calcined $Fe_2O_3^*$.

Transformation of the Supported $[Au(PPh_3)]^+$ Species upon Temperature-Programmed Calcination

At the calcination temperatures $\leq$473 K, most of adsorbed water was desorbed as proved by FT-IR in Figs. 8 and 9. Additionally, reduction of a part of Fe^{3+} to Fe^{2+} by the PPh_3-ligand was suggested to occur near 473 K in the previous report (28). However, the change was not detected by XRD and the support after calcination at 473 K was still amorphous, similar to that in $Au/Fe(OH)_3^*$ (RT). The XRD pattern of $Au/Fe(OH)_3^*$ (473 K) exhibited neither peaks for crystalline iron oxide nor Au metal phase (Fig. 2a). On the other hand, noticeable shifts of the Au 4f and P 2p peaks were observed with the $Au/Fe(OH)_3^*$ (473 K) catalyst as shown in Fig. 4. In the Au 4f region, the broadened Au $4f_{7/2}$ feature shifted to 84.1 eV by 0.8 eV, as compared to that for $Au/Fe(OH)_3^*$ (RT), which assumes partial decomposition of the gold precursor at 473 K. The broadened Au $4f_{7/2}$ and $4f_{5/2}$ peaks in the XPS spectrum of the $Au/Fe(OH)_3^*$ (473 K) can be deconvoluted as a superposition of the XPS peaks centered at 84.9 and 83.9 eV, which correspond to the initial $Au(PPh_3)(NO_3)$ complex and metallic gold, respectively, as shown in Fig. 10, where the observed spectrum was fitted by using the experimental spectra for $Au/Fe(OH)_3^*$ (RT) and $Au/Fe(OH)_3^*$ (673 K). Reliable deconvolution of the corresponding P 2p line centered at about 132.6 eV was difficult, due to low signal-to-noise ratio of the spectrum, but the BE value was close to that for triphenylphosphine adsorbed on the $Fe(OH)_3^*$ support (Table 1). Therefore, after partial cleavage of the Au-P bond, the released P species are located on the $Fe(OH)_3^*$ surface to give the P 2p BE of 132.6 eV.

EXAFS Fourier transform for $Au/Fe(OH)_3^*$ (473 K) in Fig. 5 exhibited a decrease in intensity of the Au-P peak, in comparison with that for $Au/Fe(OH)_3^*$ (RT), indicating partial decomposition of the supported Au species. The transformation of the gold precursor at 473 K was accompanied by development of the peak at about 0.27 nm in the Fourier transform. The curve-fitting analysis for the EXAFS data

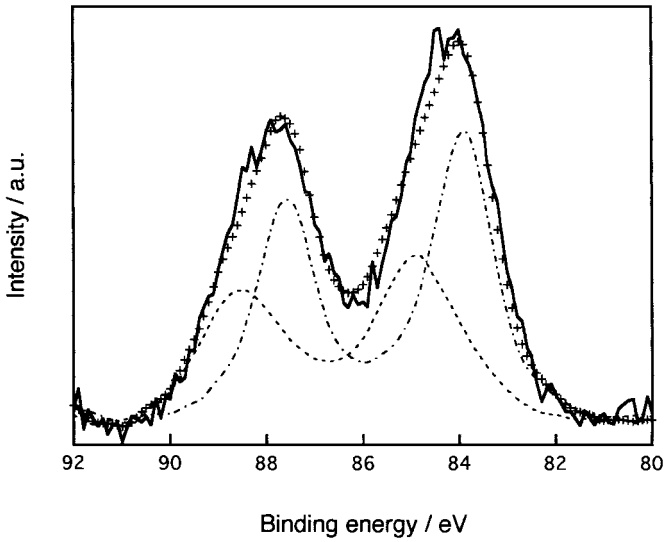

FIG. 10. Fitting of the XPS Au 4f spectrum for $Au/Fe(OH)_3^*$ (473 K): (———) observed spectrum after background removal; (+++) fitted spectrum by using the two spectra of $Au/Fe(OH)_3^*$ (RT) (-----) and $Au/Fe(OH)_3^*$ (673 K) (-·-·-).

for $Au/Fe(OH)_3^*$ (473 K) was successfully performed by using Au-P and Au-Au parameters extracted from the EXAFS data of $Au(PPh_3)(NO_3)$ and Au foil (Table 3). The coordination number for Au-Au bond was determined to be 2.2 ± 1.5, which implies the formation of three–four Au-atom clusters. However, the Au-Au bond length of 0.287 ± 0.003 nm is longer that those for gold cluster compounds such as $[Au_9(PPh_3)_8](NO_3)_3$ and $Au_{55}(PPh_3)_{12}Cl_6$ (25, 49, 50) and is characteristic of metallic gold. Additional information about the gold state in the $Au/Fe(OH)_3^*$ (473 K) catalyst was obtained from comparison of our XPS data with those for several gold(I) phosphine complexes and clusters reported by van Attekum *et al.* (51). They found that all the Au complexes and clusters have the same Au 4f binding energies with each other when they have the same ligands. Therefore, the Au-species that show the Au-Au bond of 0.287 nm and the XPS $4f_{7/2}$ peak of 83.9 eV may not be assigned to Au(I) intermediates with PPh_3 ligands which might be formed during heat decomposition of the $[Au(PPh_3)]^+$ species on the $Fe(OH)_3^*$ support.

There is general agreement in the literature that gold particles in a finely dispersed state can effectively catalyze low-temperature CO oxidation. Despite the formation of small gold metallic particles, the catalytic activity of the $Au/Fe(OH)_3^*$ (473 K) catalyst for CO oxidation was much lower than the catalysts calcined at higher temperatures as shown in Fig. 1. The importance of the composition and structure of the iron oxide support in Au/Fe-oxide catalysts has been demonstrated by several authors (27, 28, 30). As catalysts with poor crystallinity were found to exhibit a higher activity for CO oxidation, the low activity of the $Au/Fe(OH)_3^*$ (473 K) catalyst cannot be ascribed to the

amorphous state of the Fe(OH)$_3^*$ (473 K) (Fig. 2a). Possibly, the PPh_3 species released from Au(PPh_3)(NO_3) and adsorbed on the Fe(OH)$_3^*$ support at 473 K poisoned the catalytic sites. Further, active Au particles may not be efficiently distributed on the support surface at 473 K, as indicated from the Fe/Au ratio (Table 1). The Fe/Au ratio for Au/Fe(OH)$_3^*$ (473 K) was a little larger than that for Au/Fe(OH)$_3^*$ (RT), which implies that Au species in Au/Fe(OH)$_3^*$ (473 K) are located at relatively deeper pore channels below the outer surface and/or surface morphology of the Fe(OH)$_3^*$ support changed by calcination at 473 K. The oxidation of the PPh_3 to P(5+) species at the temperatures above 473 K is necessary to generate high CO oxidation activity. However, the Fe(OH)$_3^*${P} sample calcined at 673 K which showed similar P 2p BE and Fe/P ratio to those for Au/Fe(OH)$_3^*$ (673 K) did not show high oxidation activity (Fig. 1). Therefore, the P(5+) species have almost no contribution to the high activity in the low-temperature CO oxidation.

The Au/Fe(OH)$_3^*$ (573 K) sample showed drastic improvement of the activity for the low-temperature CO oxidation, in comparison with the sample calcined at 473 K. Further increase of the calcination temperature to 673 and 773 K affected the catalytic performance insignificantly as shown in Fig. 1. In contrast, the Au/$Fe_2O_3^*$ (673 K) sample showed much lower activity than the Au/Fe(OH)$_3^*$ (673 K) catalyst and also lower than the Au/Fe(OH)$_3^*$ (473 K). To find out the reasons of such difference in the catalytic performance of the samples, XRD, TEM, XPS, and EXAFS were employed. TEM photographs for Au/Fe(OH)$_3^*$ (673 K) and Au/$Fe_2O_3^*$ (673 K) revealed average Au particle sizes of 2.6 and 12 nm, respectively (Fig. 3). Intensities of the Au(111) peak in the XRD patterns for the active Au/Fe(OH)$_3^*$ (573, 673, and 773 K) catalysts were 4–6 times lower than that for the inactive catalyst Au/$Fe_2O_3^*$ (673 K) as shown in Fig. 2. The XRD patterns allowed us to suggest that gold metallic particles in the Au/Fe(OH)$_3^*$ catalysts were less than 4 nm in diameter and were not detected by XRD in agreement with the TEM results. XPS spectra for both Au/Fe(OH)$_3^*$ (673 K) and Au/$Fe_2O_3^*$ (673 K) exhibited Au $4f_{7/2}$ peak at 83.9 eV, which proves the formation of Au metallic particles. No oxidized form of gold was detected by XPS in both samples. EXAFS analysis of the Au/Fe(OH)$_3^*$ samples calcined at 573, 673, and 773 K confirmed the formation of small gold metallic particles by lower coordination numbers (7.4–8.0) for the Au-Au bond, as compared with those (12) for Au/$Fe_2O_3^*$ calcined at 473 and 673 K (Table 3). The increase of the calcination temperature from 573 to 773 K resulted in only a slight increase of the coordination number from 7.4 ± 1.0 to 8.0 ± 1.0, which demonstrates the stability of the gold dispersion in Au/Fe(OH)$_3^*$ under the high-temperature calcination. In contrast, as for the Au/$Fe_2O_3^*$ sample, calcination even at 473 K produced large gold metallic particles with the large coordination number of 12 ± 1.0, similar to Au foil (Table 3). The results indicate weak or negligible interaction of the Au complex precursor with the $Fe_2O_3^*$ support. No evidence on the presence of oxidized forms of gold in the Au/Fe(OH)$_3^*$ samples was found by the XPS and EXAFS analyses. Additionally, no XRD peaks in the 2θ region of 5–15° that could be prescribed to the formation of supercluster structures (52) were observed during the Au(PPh_3)(NO_3) decomposition on the Fe(OH)$_3^*$ support. In consequence, it may be concluded that small Au metallic particles are a gold phase responsible for the high activity of the Au/Fe(OH)$_3^*$ catalysts for the low-temperature CO oxidation.

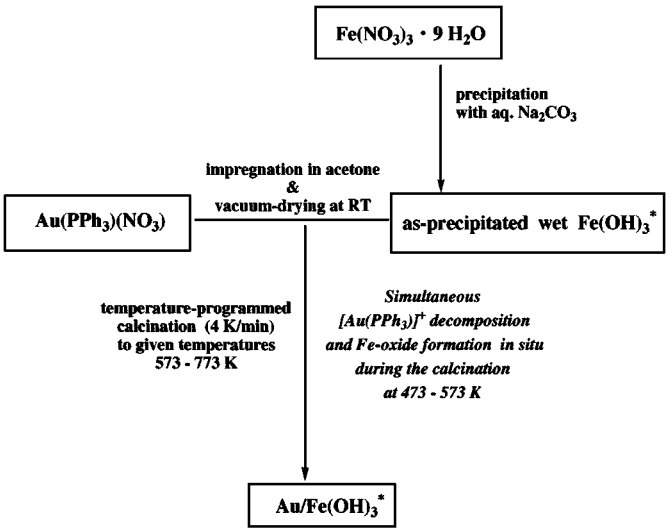

SCHEME 1. Preparation steps for the active Au/Fe(OH)$_3^*$ catalysts.

Thus, it was found that during calcination of the Au/Fe(OH)$_3^*$ samples, the [Au(PPh_3)]$^+$ species that strongly interacted with the Fe(OH)$_3^*$ oxide-precursor decomposed to small Au metallic particles at 473–573 K. Formation of the highly defective iron oxide support consisting of α-Fe_2O_3 and γ-Fe_2O_3 was detected in almost the same temperature range (28), as shown in Scheme 1. The simultaneous occurrence of the two transformation processes seems to be most relevant to the formation of small Au metallic particles dispersed on the oxide support for high catalytic performance for the CO oxidation.

CONCLUSIONS

The behaviors of the Au(PPh_3)(NO_3) precursor upon supporting on the as-precipitated wet Fe(OH)$_3^*$, as well as during the temperature-programmed calcination to different temperatures, were studied by means of FT-IR, XRD, TEM, XPS, and EXAFS and compared with catalytic CO oxidation activities of the samples. The following conclusions are drawn by the combined data:

(1) Dissociation of the gold precursor on the Fe(OH)$_3^*$ surface to produce [Au(PPh_3)]$^+$ species strongly interacting

with the support surface as suggested by FT-IR is the first step in the formation of highly dispersed gold particles.

(2) Higher stability of the $Au(PPh_3)(NO_3)$ complex on the $Fe(OH)_3^*$, as compared with that on the $Fe_2O_3^*$ was demonstrated by EXAFS.

(3) It was found that calcination of the $Au/Fe(OH)_3^*$ sample at $\geq$573 K produced highly active catalysts for low-temperature CO oxidation. Decomposition of the phosphine-ligated gold complex $Au(PPh_3)(NO_3)$ on the $Fe(OH)_3^*$ support at $\geq$573 K led to the formation of small and stable gold metallic particles.

(4) The occurrence of both the $[Au(PPh_3)]^+$ decomposition to Au metallic particles and the transformation of the $Fe(OH)_3^*$ to Fe oxides in almost the same temperature range 473–573 K seems to be most relevant to the formation of stabilized small Au metallic particles in the case of gold-phosphine precursors.

(5) No evidence was found by XPS and EXAFS on the presence of oxidized forms of gold and stable cluster structures in the $Au/Fe(OH)_3^*$ samples with the high activity for the CO oxidation.

ACKNOWLEDGMENT

This work has been supported by Core Research for Evolutional Science and Technology (CREST) of Japan Science and Technology Corporation (JST).

REFERENCES

1. Huber, H., McIntosh, D., and Ozin, G. A., *Inorg. Chem.* **16**, 975 (1977).
2. Haruta, M., Kobayashi, T., Sano, H., and Yamada, N., *Chem. Lett.*, 405 (1987).
3. Haruta, M., Yamada, N., Kobayashi, T., and Iijima, S., *J. Catal.* **115**, 301 (1989).
4. Haruta, M., Tsubota, S., Kobayashi, T., Kageyama, H., Genet, M. J., and Delmon, B., *J. Catal.* **144**, 175 (1993).
5. Andreeva, D., Idakiev, V., Tabakova, T., and Andreev, A., *J. Catal.* **158**, 354 (1996).
6. Andreeva, D., Idakiev, V., Tabakova, T., Andreev, A., and Giovanoli, R., *Appl. Catal. A: General* **134**, 275 (1996).
7. Sakurai, H., Ueda, A., Kobayashi, T., and Haruta, M., *Chem. Commun.*, 271 (1998).
8. Sakurai, H., and Haruta, M., *Appl. Catal. A: General* **127**, 93 (1995).
9. Haruta, M., Ueda, A., Tsubota, S., and Torres-Sanchez, R. M., *Catal. Today* **29**, 443 (1996).
10. Liu, W., and Flytzani-Stephanopulos, M., *J. Catal.* **153**, 304 (1995).
11. Liu, W., and Flytzani-Stephanopulos, M., *J. Catal.* **153**, 317 (1995).
12. Torres-Sanchez, R. M., Ueda, A., Tanaka, K., and Haruta, M., *J. Catal.* **168**, 125 (1997).
13. Hutchings, G. J., Siddiqui, M. R. H., Burrows, A., Kiely, C. J., and Whyman, R., *J. Chem. Soc., Faraday Trans.* **93**, 187 (1997).
14. Gardner, S. D., Hoflund, G. B., Schryer, D. R., Schryer, J., Upchurch, B. T., and Kielin, E. J., *Langmuir* **7**, 2135 (1991).
15. Hoflund, G. B., Gardner, S. D., Schryer, D. R., Upchurch, B. T., and Kielin, E. J., *Appl. Catal. B: Environ.* **6**, 117 (1995).
16. Baiker, A., Maciejewski, M., Tagliaferri, S., and Hug, P., *J. Catal.* **151**, 407 (1995).
17. Salama, T. M., Ohnishi, R., Shido, T., and Ichikawa, M., *J. Catal.* **162**, 169 (1996).
18. Bamwenda, G. R., Obuchi, A., Atsushi, O., Junko, O., Kushiyama, S., and Mizuno, K., *J. Mol. Catal. A: Chemical* **126**, 151 (1997).
19. Iwasawa, Y. (Ed.), "Tailored Metal Catalysts." Reidel, Dordrecht, 1986.
20. Gates, B. C., *Chem. Rev.* **95**, 511 (1995).
21. Schwarz, J. A., Contescu, C., and Contescu, A., *Chem. Rev.* **95**, 477 (1995).
22. Ichikawa, M., *Adv. Catal.* **38**, 283 (1992).
23. Graf, I. V. G., Bacon, J. W., Consugar, M. B., Curley, M. E., Ito, L. N., and Pignolet, L. H., *Inorg. Chem.* **35**, 689 (1996).
24. Yuan, Y., Asakura, K., Wan, H., Tsai, K., and Iwasawa, Y., *Chem. Lett.*, 129 (1996).
25. Yuan, Y., Asakura, K., Wan, H., Tsai, K., and Iwasawa, Y., *J. Mol. Catal. A: Chemical* **122**, 147 (1997).
26. Yuan, Y., Asakura, K., Wan, H., Tsai, K., and Iwasawa, Y., *Chem. Lett.*, 755 (1996).
27. Yuan, Y., Kozlova, A. P., Asakura, K., Wan, H., Tsai, K., and Iwasawa, Y., *J. Catal.* **170**, 191 (1997).
28. Kozlova, A. P., Sugiyama, S., Kozlov, A. I., Asakura, K., and Iwasawa, Y., *J. Catal.* **176**, 426 (1998).
29. Mathieson, T. J., Langdon, A. G., Milestone, N. B., and Nicholson, B. K., *Chem. Commun.*, 371 (1998).
30. Hutchings, G. J., Siddiqui, M. R. H., Burrows, A., Kiely, C. J., and Whyman, R., *J. Chem. Soc., Faraday Trans.* **93**, 187 (1997).
31. Minico, S., Scire, S., Crisafulli, C., Visco, A. M., and Galvagno, S., *Catal. Lett.* **47**, 273 (1997).
32. Haruta, M., *Catal. Today* **36**, 153 (1996).
33. Boccuzzi, F., Guglielminotti, E., Pinna, F., and Strukul, G., *Surf. Sci.* **377–379**, 728 (1997).
34. Iwasawa, Y., *Stud. Surf. Sci. Catal. (Proc. 11th Int. Congr. Catal. Baltimore)*, Vol. 101, p. 21. Elsevier, Amsterdam/New York, 1996.
35. Iwasawa, Y., *Catal. Today* **18**, 21 (1993).
36. Bruce, M. I., Nicholson, B. K., and Shawkataly, O. B., *in* "Inorganic Syntheses" (H. D. Kaesz, Ed.), Vol. 26, p. 324. Wiley, New York, 1989.
37. Mueting, A. M., Alexander, B. D., Boyle, P. D., Casalnuovo, A. L., Ito, L. N., Johnson, B. J., and Pignolet, L. H., *in* "Inorganic Syntheses" (R. N. Grimes, Ed.), Vol. 29, p. 280. Wiley, New York, 1992.
38. Wagner, C. D., Riggs, W. M., Davis, L. E., Moulder, J. F., and Mullenberg, G. E. (Eds.), "Handbook of X-ray Photoelectron Spectroscopy: A Reference Book of Standard Data for Use in X-Ray Photoelectron Spectroscopy." Perkin-Elmer, Eden Prairie, MN, 1979.
39. "Handbook of X-ray Photoelectron Spectroscopy." JEOL, Tokyo, 1991.
40. Iwasawa, Y. (Eds.), "X-ray Absorption Fine Structure for Catalysts and Surfaces." World Scientific, Singapore, 1996, p. 33.
41. Barron, P. F., Engelhardt, L. M., Healy, P. C., Oddy, J., and White, A. H., *Aust. J. Chem.* **40**, 1545 (1987).
42. Lee, J. S., Kim, S., and Kim, Y. G., *Top. Catal.* **2**, 127 (1995).
43. Guglielminotti, E., and Boccuzzi, F., *Appl. Catal. B: Environ.* **8**, 375 (1996).
44. Pouchert, C. J., "The Aldrich Library of Infrared Spectra." Aldrich Chem. Co., Milwaukee, WI, 1975.
45. Dolphin, D., and Wick, A., "Tabulation of Infrared Spectral Data." Wiley, New York, 1977.
46. Lorenzelli, V., Rossi, P. F., Busca, G., and Cotena, N., *Heterog. Catal., Proc. Int. Symp., 1979*, 4th, Pt. 1, 463.
47. Tsyganenko, A. A., and Filimonov, V. N., *Spectrosc. Lett.* **5**, 477 (1972).
48. Kozlov, A. I., Kozlova, A. P., Liu, H., and Iwasawa, Y., *Appl. Catal. A: General*, in press.
49. Hall, P. K., and Mingos, M. P., *in* "Progress in Inorganic Chemistry" (S. J. Lippard, Ed.), Vol. 32, p. 237. Wiley, New York, 1984.
50. Marcus, M. A., Andrews, M. P., Zegenhagen, J., Bommannavar, A. S., and Montano, P., *Phys. Rev. B* **42**, 3312 (1990).
51. van Attekum, P. M. Th. M., van der Velden, J. W. A., and Trooster, J. M., *Inorg. Chem.* **19**, 701 (1980).
52. Schmid, G., and Klein, N., *Angew. Chem. Int. Ed. Engl.* **25**, 922 (1986).